

DE-EE0006816.0000
Oregon State University
Advanced Laboratory and Field Arrays (ALFA) for Marine Energy

1. INTRODUCTION

Soil-structure interaction has been an area of active research since the 19th century and has evolved significantly over the past 150 years (Kausel, 2010). Previous soil-structure interaction studies have been based on numerical simulations (e.g., Costantino et al. 1976; Jensen et al. 1999; Jensen, Edil et al. 2001; Jensen, Plesha et al. 2001; Dove et al. 2006; Wang, 2006; Wang, Dove, and Gutierrez, 2007a, 2007b; Wang, Gutierrez, and Dove, 2007) and/or physical experiments (e.g., Uesugi and Kishida 1986a, 1986b, 1988; Hu and Pu 2004;). The majority of the previous research has employed either the finite element method (FEM) or the boundary element method for numerical studies of soil-structure response (e.g., Costantino et al. 1976; Hall and Oliveto 2003; Kuppusamy et al. 1992; Cheng 1989). These methods both consider the soil medium as a continuum, which can have certain drawbacks, particularly when robust simulation of post-peak softening is required.

The discrete element method (DEM), however, allows for the simulation of soils as a collection of individual particles (Cundall and Strack 1976) and is increasingly being applied to a wide array of problems that involve granular materials in contact with a geostructure (e.g., Kress and Evans 2010; Evans and Kress 2011). DEM models predict the emergent behavior of particulate assemblies (e.g., sands) based on simulation of independent particle behaviors. Because DEM simulations are capable of predicting emergent phenomena, they have been successfully applied to the study of shear bands in sand, including free-field granular-granular shearing (Jacobsen et al. 2007; Evans and Frost 2010; Zhao and Evans 2011; Frost et al. 2012) and also granular-continuum interface shearing (Hall and Oliveto 2003; Dove et al. 2006; Wang, Gutierrez, and Dove 2007; Wang, Dove, and Gutierrez 2007b; Kress and Evans 2010; Evans and Kress 2011; Wang and Jiang 2011). Using DEM simulations, previous researchers have modeled the shear banding behaviors of particulate assemblies and the influence of particle (e.g., grain size distribution, roughness, roundness) or continuum counterface (e.g., interaction topography, surface stiffness) properties on shearing response. Dove et al. (2006) and Wang et al. (2007) used asperity angle, asperity slope, asperity peak, and asperity spacing to quantify the interfaces. Jacobsen et al. (2007) and Wang and Jiang (2011) have used DEM models to assess boundary effects on the formation of shear bands. Overall, simulated material response from DEM simulations have been shown to be consistent with results from physical experiments for a variety of loading conditions (Zhao and Evans 2009; Evans and Frost 2010).

In marine systems, the interaction between seabed sands and offshore anchors is one specific example of soil-structure interaction. The basic analysis principles for these systems are generally consistent with those for soil-structure interactions for onshore applications, such as those discussed previously. In the case of marine hydrokinetic (MHK) energy generators, however, these anchors serve not only to keep the devices on station, but also as the reaction force necessary for energy generation. The holding capacity of the anchors must bear the tensile force from ocean waves transmitted by mooring lines. For a catenary mooring system, the mooring line has an inclination angle with the seabed and will apply both vertical

and horizontal forces to the anchor. The properties of the seabed and the anchor combine to determine the holding capacity and allowable reaction force for a given anchor design. Much of the previous work on offshore anchors has focused on FEM analyses and/or limit equilibrium solutions (Lieng et al. 2000; O’Loughlin et al. 2013; O’Beirne et al. 2015). However, both of these approaches neglect much of the fundamental physics occurring at the anchor-soil interface, and thus, may be unsuitable for assessing the potential for anchor-soil interface softening in MHK systems. The current work employs DEM simulations using the software *PFC^{3D}* (Itasca 2008) to evaluate the effects of soil properties and anchor surface roughness on holding capacity.

2. PRELIMINARY LITERATURE REVIEW

2.1. Granular-Continuum Interface Behavior

2.1.1. Physical Studies

Offshore anchors interact intimately with the sediments around them. Anchor self-weight and soil-anchor interface shear forces provide holding capacity for an MHK device. Similar to other soil-structure interactions, soil-anchor interaction is a function of counterface properties as well as soil properties. Anchor surface roughness, particle mineralogy, and the stress state of the seabed soil are examples of the factors that control anchor holding capacities. Physical and numerical experiments have been used by previous researchers to investigate this interplay between granular and continuum systems.

Yoshimi and Kishida (1981) used ring shear tests to evaluate the friction between soil and a metal surface. They evaluated the friction between sand and steel surfaces for a range of surface roughness and soil densities. From their tests, they found that the shear stress ratio and volumetric strain are not affected by the surface roughness of the steel surface during initial loading. The tangential displacement consists mostly of slip for smooth surfaces and mostly shear distortion for very rough surface. The overall coefficient of friction for the granular-continuum system was found to be governed primarily by the metal surface roughness.

The relationship between the ratio of shear stress to normal effective stress, τ/σ' , and sliding displacement, δ , has been previously studied for sand-continuum interfaces using physical direct shear experiments. Uesugi and Kishida (1986b and, 1988) described a method for observing the particle behavior near the soil-steel interface during testing. They found that the sand type and the surface roughness of the steel were more influential in determining the interface shear strength than the applied normal effective stress (σ') and the mean grain size, d_{50} . In addition, the rolling of particles along the interface plays an important role in the friction. When the shear stress ratio, τ/σ' , of the shear zone is smaller than the coefficient of friction at yield, μ_y , this value becomes the upper-limiting value of coefficient of friction.

Uesugi and Kishida (1986a) proposed a normalized surface roughness which is defined as maximum surface roughness normalized by the mean grain size. The roughness of the steel surface is given as:

$$R = R_{\max(L=d_{50})} \quad (1)$$

and the normalized roughness is then:

$$R_n = \frac{R_{\max(L=d_{50})}}{d_{50}} \quad (2)$$

where R_{\max} is evaluated for a gage length of $L = d_{50}$.

Uesugi and Kishida (1986a) also found that the maximum shear stress ratio of a medium dense sand has a lower value than that of a very dense sand. The relationship between shear stress ratio at yield and normalized roughness is not affected by d_{50} . They developed an empirical approximation of the shear stress ratio at yield that relies upon particle shape and counterface roughness:

$$\mu_y = \frac{1}{\bar{R}} (A + B \cdot R_n) \quad (3)$$

where A and B are constants influenced by the adhesive shear resistance of interfaces. \bar{R} is the modified roundness, calculated as:

$$\bar{R} = \frac{(R_1 + R_2 + \dots + R_M)}{M} \quad (4)$$

Generally, \bar{R} is taken as the average roundness of 70-100 particles.

Hu and Pu (2004) proposed a damage model to predict soil-interface shear behavior. They also performed a series of direct and simple shear tests and FEM simulations for verifications. The model incorporated the maximum surface roughness proposed by Uesugi and Kishida (1986a) and given in Eq. 1. Hu and Pu (2004) suggested that there is a critical relative roughness R_{cr} that serves as the line of demarcation between rough and smooth. Based on the counterface roughness category, the interface failure model can be classified as elastic perfect plastic with little dilatancy ($R < R_{cr}$) or as strain localizing with shear zone formation ($R > R_{cr}$). They develop a damage model based on disturbed state concept to simulate the stress-strain relationship of a rough soil-structure interface. The material can be considered as two different states: intact and critical state. During shearing, the state will evolve from intact state to critical state due to microstructural changes. They constructed a damage function to describe this behavior:

$$D = 1 - e^{-a \cdot \xi^b} \quad (5)$$

where D is the damage function which equals zero at the beginning of shearing and 1.0 as the system approaches critical state, and

$$\xi = \int (d\varepsilon_s^p \cdot d\varepsilon_s^p)^{1/2} \quad (6)$$

is the trajectory of plastic shear strain, in which $d\varepsilon_s^p$ is plastic shear strain, and a and b are empirical coefficients determined from physical tests. The damage function can also be defined in terms of shear stress of intact and critical states as:

$$D = \frac{\tau^i - \tau}{\tau^i - \tau^c} \quad (7)$$

where τ^i and τ^c are shear stress at the intact and critical states, respectively.

Evgin and Fakharian (1996) developed an apparatus to perform two- and three-dimensional tests that facilitate sliding displacement at the interface and shear deformation in the soil mass. They conducted physical experiments to study the behavior of an interface between a rough steel surface and dense sand and evaluated the shear stresses in both lateral directions when normal stress was applied vertically. Two and three dimensional constant normal stress and stiffness tests were performed to investigate the influence of different stress paths on the stress displacement relations of an interface. They found that the shear stress ratios at peak and residual states were independent of stress path; however, the stress path significantly influences the shear stress-tangential displacement and volume change behavior at the interface. Sliding displacement at the interface and the shear deformation of the sand mass were observed to be plastic.

Dove and Jarrett (2002) used a series of physical experiments to investigate how surface topography influences the interface strength and deformation behavior. They defined the surface geometry parameters, root spacing S_r , asperity spacing, and asperity angle to quantify the surface topography. The parameters are illustrated in Figure 1.

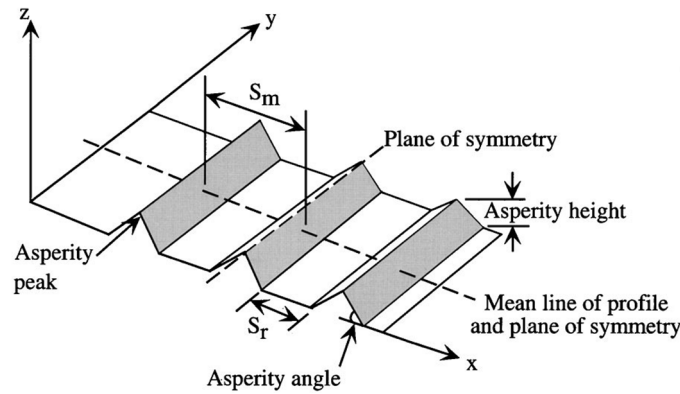


Figure 1. Description of a rough surface (after Dove and Jarret 2002).

Direct interface shear tests were performed on the surface by using Ottawa 20-30 sands and glass microbeads to evaluate how surface topography controls the behavior of interfaces between particulate soils and idealized material interfaces. They investigated the interface strengths in terms of a normalized efficiency parameter (E) which is defined in Equation 8 as:

$$E = \frac{\tan \delta}{\tan \phi'} \quad (8)$$

where $\tan \delta$ is interface friction coefficient and $\tan \phi'$ is granular material friction coefficient. Efficiency varies from nearly zero to one from low strength to full strength conditions, respectively. They found if the ratio between asperity heights and mean grain size is larger than 0.9, and the asperity angle is less than 60° , the interface has steady-state strength which is independent of spacing. If the asperity angle is 60° , efficiency decreases rapidly when the ratio of spacing to mean grain size is larger than 3.0.

In addition to interface roughness and topography, sand friction, sand stiffness, wall friction and wall stiffness are also important for interface shear behavior. Different construction materials correspond to different frictions and interface stiffnesses. Potyondy (1961) studied the skin friction between various soils and different construction materials. In the test, the skin friction between three different construction

materials and various soils were determined by performing two kinds of experimental tests – strain controlled and stress controlled shear tests. He expressed the resulting stress-strain response as an exponential equation of displacement:

$$\frac{\tau}{\sigma} = \tan \delta \left[1 - \exp \left(-k \frac{s}{s_0 - s} \right) \right] \quad (9)$$

where τ is the shearing stress that produces s displacement, σ is the normal stress, δ is the angle of interface friction, s_0 is the displacement at failure and k is a constant for a given soil. The higher the interface stiffness, the lower the skin friction (note that this was later observed numerically by Frost et al., 2002). Potyondy (1961) also demonstrated that the rougher the interface, the higher the skin friction. The interface friction angle is unlimited, but system strength approaches the friction angle of the adjacent soil.

Given the importance of particulate-continuum interface behaviors and their influence on the response of geostuctures, understanding the localized shearing mechanisms governing the behavior is necessary. Frost et al. (2002) performed physical experiments and complimentary numerical simulations to assess the interplay of roughness and hardness on interface strength. They performed tests on a set of continuum materials with different surface roughnesses and hardnesses. Rather than the normalized surface roughness measure employed by Uesugi and Kishida (1986b), they elected to use the average surface roughness as follows:

$$R_a = \frac{1}{L} \int_0^L |z| dx \quad (10)$$

where R_a is average roughness, L is the sample length and z is the absolute height from the mean line. They performed interface shear tests on different continuum materials and their interaction with Ottawa sand and Valdosta blasting sand. Their measurements showed that the interface friction angle will decrease with the increasing of surface hardness and will increase with increasing surface roughness.

Dove, et al. (2006) explored the steady state strength of particle-scale roughness non-dilative interface systems by experimentally testing interfaces between glass beads and natural subrounded quartz sands and surface materials like high-density polyethylene, polyvinylchloride, fiber reinforced plastic, stainless steel, and heat-treated steel. They found the initial peak and steady state friction coefficients depend not only on the grain properties, but interface properties. Grain shape, relative hardness of the mating materials and normal load were found to control the stress-displacement and strength behavior.

Dove, et al. (1999) studied the peak friction behavior of smooth geomembrane-particle interface behavior using a custom designed shear apparatus. The shear mechanisms at Ottawa 20-30 sand-high density polyethylene (HDPE) geomembrane interfaces were investigated using contact mechanics, tribology, and basic friction theory. Sliding and plowing were found to be the major factors governing interface shear behavior. Plowing results in an increasing of friction coefficient and will increase the normal stress. Sliding will increase contact area and flatten the peak strength envelope. The dominant component is changing with the normal stresses shown in Figure 2. Sliding dominates the friction if the normal stress is under 50 kPa while plowing dominates the friction when normal stress larger than 50 kPa.

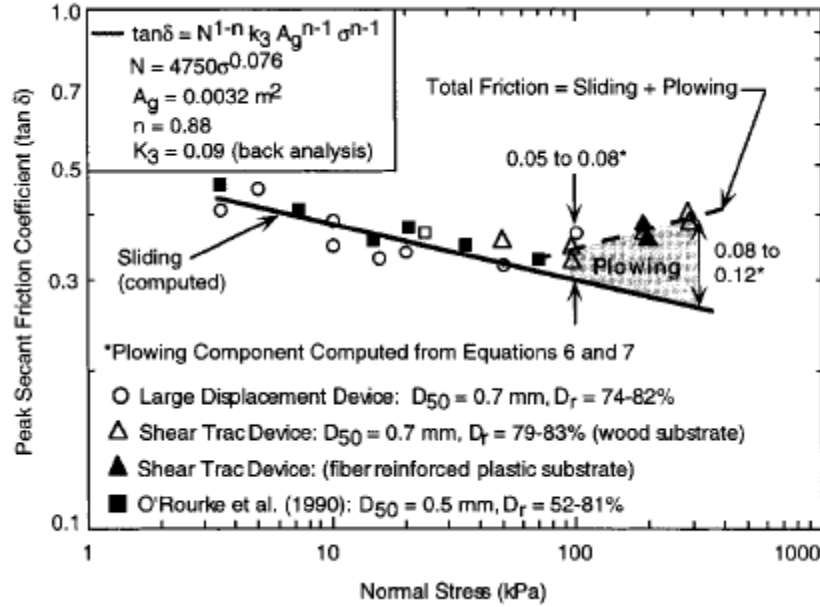


Figure 2. Geomembrane-Ottawa sand interface shear Mechanism (after Dove, et al. 1999)

Kulhawy and Peterson (1979) investigated sand-concrete interface behaviors with an extensive testing program to examine the strength and stress-deformation response. They examined the effects of interface roughness and soil gradation. The interface friction angle for rough counterface materials was found to be equal to or greater than the soil internal friction angle. Failure was observed to occur inside the soil away from interface. Smooth interfaces had friction angles smaller than the soil internal friction angle, indicating failure at the soil-continuum interface. They defined the relative roughness of a soil-continuum interface system as:

$$R_R = \frac{R_{structural_face}}{R_{soil}} \quad (11)$$

where R_R is the relative roughness of the interface and $R_{structural_face}$ and R_{soil} are the interface and soil roughnesses respectively. $R_R > 1$ is defined as a rough interface while $R_R < 1$ is defined as a smooth interface.

In general, practical problems involve the interaction of different types of soils with different construction materials. Reasonable interface properties serve to guide the construction practices and provide inputs to numerical analyses such that it is possible to reach meaningful solutions. To this end, Acar, et al. (1982) performed experiments to estimate the effects of material and state parameters on interface behavior. Tests of quartz sand interacting with three different construction materials, steel, wood and concrete at varying normal effective stresses were selected to assess skin friction. The results from the physical experiments were used to develop parameters for a hyperbolic model (Clough and Duncan 1969), as shown in Equation 12:

$$\frac{\Delta_s}{\tau} = b + a\Delta_s \quad (12)$$

where τ is shear stress, Δ_s is shear displacement, and a and b are interface constants that depend on the roughness and normal stress, σ_n . The initial tangent stiffness, K_{si} , is given as $1/b$ at small displacements and $1/a$ is the ultimate shear stress, τ_{ult} . A failure ratio R_f is defined by the shear strength at failure, τ_f , and the ultimate shear stress, τ_{ult} :

$$R_f = \frac{\tau_f}{\tau_{ult}} \quad (13)$$

The nonlinear, stress-dependent tangent shear stiffness, K_{st} , of different construction materials with different initial tangent shear stiffnesses are represented as:

$$K_{st} = \frac{\partial \tau}{\partial \Delta_s} = K_{si} \left(1 - \frac{R_f}{\sigma_n \tan \delta} \right)^2 \quad (14)$$

$$K_{si} = K_j \gamma_w \left(\frac{\sigma_n}{p_a} \right)^n \quad (15)$$

where p_a is atmospheric pressure, K_j is shear stiffness at $\sigma_n = p_a$, and δ is the skin friction angle. While the above formulation can reasonably model the actual stress-displacement behavior of a soil-continuum interface, it provides little insight into the underlying particle physics, thus making extrapolation to other systems difficult and uncertain.

2.1.2. Numerical Studies

In addition to the physical tests discussed previously, there have also been limited numerical studies of granular-continuum interface behavior, with DEM modeling being the most common approach (e.g., Jensen, et al., 1999; Jensen, et al., 2001a; Jensen, et al., 2001b). Numerical studies specifically of shear banding at the interface was studied by Wang, et al. (2007).

Jensen et al. (1999, 2001a, 2001b) studied two-dimensional interfaces using DEM simulations. They noted that interface shear and a slipzone will result when the soil-structure system deforms. They model a particle of general shape by combining many smaller particle of simple shapes into a single larger, more complex particle which can closely simulate the real particle behaviors, e.g., particle interlock (Figure 3). However, the interface is only a few particle diameters. They investigate behaviors such as particle rotations, relative grain displacements, and grain crushing and their influences on interface behavior.

Theoretically, combining a large number of smaller circular particles into larger clusters can more accurately simulate real particle shapes. Jensen et al. (1999) simulated the effectiveness of clustered particles and simple circular particles to investigate their influence on interfacial phenomena. They built a sawtooth wall as the shearing surface, and changed the surface roughness by changing the relationship between sawtooth lengths with non-clustered particle diameter, λ . During their simulation, four shearing surfaces were investigated with the adjustment of different normal stresses. Dilation was measured by recording normal displacement of top wall at constant stress. Surface roughness and particle shapes and their influences on interface behavior were evaluated. The higher the surface roughness, the larger the tangential force required for failure. Clustered particles had a higher tangential force than non-clustered particle under same normal stress.

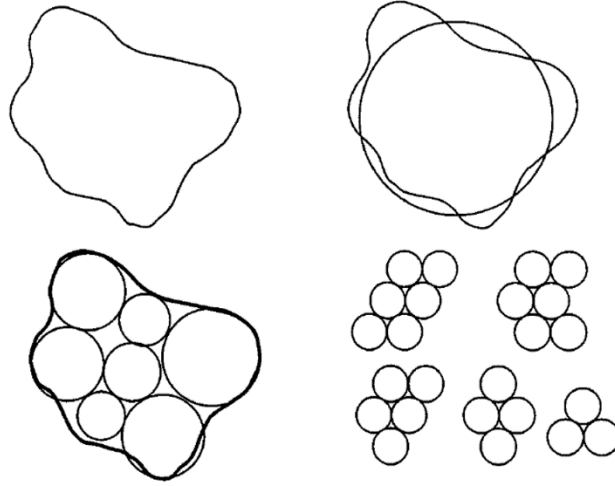


Figure 3. Outline of particle shapes used by Jensen, et al. (1999, 2001a, 2001b).

Jensen, et al. (2001b) performed two-dimensional DEM simulations of particle damage at the continuum counterface. They treated particle crushing as the breakdown of bound clusters (e.g., Figure 2). They observed an obvious distinct shear zone adjacent to the continuum. They found that there is a small decrease in peak shear stress with damage when compared to a system wherein particles are not allowed to crush. The magnitude of the steady state shear stress is lower in damaged cluster assembly compared with the undamaged cluster assembly. Constant stress and constant volume tests were performed and shear and normal forces were found to be larger in the constant volume tests than in constant stress tests. Particle damage was shown to play a strong role in the formation of the shear zone.

Additionally, Jensen, et al. (2001a) used two-dimensional DEM simulations to investigate the effect of particle shape on void ratio and interface friction. Simulation results showed that the void ratio of the assembly increases with the increasing particle angularity and particle roughness. The interface shear strength also increased with increasing angularity and roughness. The roughness was defined as in equation 16:

$$R = \frac{P}{P_{en}} \quad (16)$$

where P is perimeter of the cluster and P_{en} is the enclosed perimeter of cluster. Angularity was defined as:

$$A_i = (180^\circ - a) \frac{x}{r'} \quad (17)$$

where A_i is the degree of angularity of each corner, a is measured angle of lines which are drawn from a corner and tangent to the inscribed circle, r' is the radius of the maximum inscribed circle, and x is the distance to the tip of the corner from the center of the maximum inscribed circle. The values of degree of angularity are used to define the roundness of the particle. When $A < 300$, the particle is considered to be rounded; $300 < A < 600$ corresponds to sub-rounded; $600 < A < 900$ is sub-angular; and $A > 900$ was considered to be angular.

Wang et al. (2007) performed two-dimensional DEM simulations to study of shear band formation in interface direct shear tests. They simulated the strain localization of an idealized interphase assembly

consisting of densely packed spherical particles adjacent to a rough surface. In their study, they proposed a new strain calculation method to generate the strain field inside a shear box. The surface was built with regular and irregular parts. The irregular surface was used to simulate the rough counterface and the regular smooth surface placed at the ends of the box was to avoid boundary effects.

Soil-structure interaction occurs at the interface between two interphases. Among all the behaviors at the interface, interface shear strength is the most critical. Wang, et al, (2007a) present an anisotropy-based failure criterion to estimate the shear strength at the interface. The anisotropy-based methodology is based on the contact force anisotropy that develops in the interface region. Here, anisotropy means specifically the deviation of contact and contact force orientation from their isotropic state. The parameters used in their work are based on two-dimensional DEM simulations of an interface direct shear test. The magnitude and direction of the average contact force at the interface controls the shear strength. They present a failure criterion relating the direction of the surface normal distribution θ_a to the shear strength. Second-order tensors of contact force anisotropies for two dimensional assemblies of disks were originally derived by Rothenburg (1980):

$$N_{ij} = \frac{1}{2\pi} \int_0^{2\pi} \frac{\bar{f}_n(\theta)}{\bar{f}_0} n_i n_j d\theta = \frac{1}{N_c} \sum_{k=1}^{N_c} \frac{f_n^k}{\bar{f}_0} n_i^k n_j^k \quad (18)$$

$$S_{ij} = \frac{1}{2\pi} \int_0^{2\pi} \frac{\bar{f}_s(\theta)}{\bar{f}_0} n_i n_j d\theta = \frac{1}{N_c} \sum_{k=1}^{N_c} \frac{f_s^k}{\bar{f}_0} t_i^k n_j^k \quad (19)$$

where N_{ij} and S_{ij} are average contact normal and shear force tensors, $\bar{f}_n(\theta)$ and $\bar{f}_s(\theta)$ are density distribution functions, f_n^k and f_s^k are contact normal and shear force, respectively, $\mathbf{n} = [\cos\theta, \sin\theta]$ is the unit contact normal force, $\mathbf{t} = [-\sin\theta, \cos\theta]$ is the vector perpendicular to \mathbf{n} , N_c is the number of particle contacts in the assembly, and \bar{f}_0 is the average contact force, which can be calculated as:

$$\bar{f}_0 = \frac{1}{2\pi} \int_0^{2\pi} \bar{f}_n(\theta) d\theta = \frac{1}{N_c} \sum_{k=1}^{N_c} f_n^k \quad (20)$$

Second-order Fourier series approximations for $\bar{f}_n(\theta)$ and $\bar{f}_s(\theta)$ were proposed by Bathurst and Rothenburg (1990) as follows:

$$\bar{f}_n(\theta) = \bar{f}_0 [1 + a_n \cos 2(\theta - \theta_n)] \quad (21)$$

$$\bar{f}_s(\theta) = \bar{f}_0 [-a_s \sin 2(\theta - \theta_s)] \quad (22)$$

where a_n and a_s are corresponding to the eigenvalues of normal and shear contact force tensors, θ_n and θ_s are related to the principal directions of these contact force anisotropies measured from the actual mechanical interaction between surface asperities and granular material which can only be obtained from DEM simulations.

The failure criterion of interphase systems built by Wang et al (2007) is related to the parameters described above. Additionally, a criterion based on an efficiency parameter is described. Peak efficiency is defined by peak effective stress friction coefficient from direct interface shear tests and peak effective

stress friction coefficient of the granular material alone. It is the magnitude and direction of the average contact force that control the interface strength behavior.

Wang et al., (2007b) used a discrete-continuum approach to examine the direct shear test. In strain computation, unlike the general spatial discretization and the higher-order, non-local, mesh-free method put forward by O'Sullivan et al. (2003), they put forward a modified mesh-free method that can be used to calculate the displacement gradient directly based on movements of individual particles. The general spatial discretization method does not consider particle rotations, which are known to play an important role in shear banding; however, the use of a linear local interpolation function in the mesh-free method described by O'Sullivan et al. (2003) does not smooth the displacement gradient within the shear band. The modified mesh-free method does not use interpolation functions and calculates the displacement gradient directly based on individual particle movements. Importantly, Wang et al., (2007b) found that the effects of non-coaxiality are minor for granular material at peak state.

2.2. Offshore Dynamically Penetrated Anchors

There are multiple variations of wave energy converters, either in designs or concepts. For example, *attenuator*, *point absorber*, *terminator*, *submerged pressure differential* and *overtopping device* are all floating wave energy converters. To use wave energy for electricity generation, the WECs above must be anchored to the seabed and moored by cables. Drew et al. (2009) provides a nice overview of the literature on wave energy converter technology.

Multiple anchor types are currently employed in offshore engineering applications. For the following work, a dynamically penetrated anchor (DPA) (Figures 4 and 5) is the predominant style for analysis. These anchors penetrate into the seabed using self-weight under free-fall (Randolph and Gourvenec, 2011). DPAs are simple to design and economical to fabricate.

For the DPAs, prediction of the penetration depth is a key aspect in determining the ultimate holding capacity. The holding capacity is dominated by fluid drag resistance at shallow depths and shearing resistance at further depths (Randolph and Gourvenec, 2011). Depth of penetration is also importantly used to determine the confining stress in numerical simulations and limit equilibrium calculations. The penetration depths is expected to be 2-3 times of the anchor length, resulting in a holding capacity of 3-5 times the anchor weight. Penetration depths rely mainly on the impact velocity of the anchors.

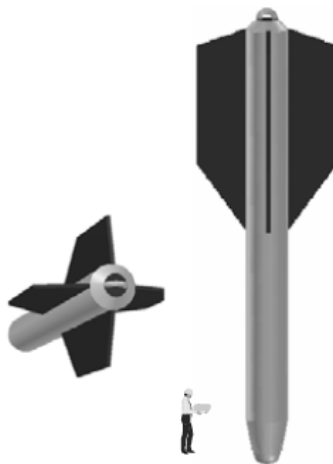


Figure 4. Deep penetrating anchor diagram (after Lieng, et al. 1999).

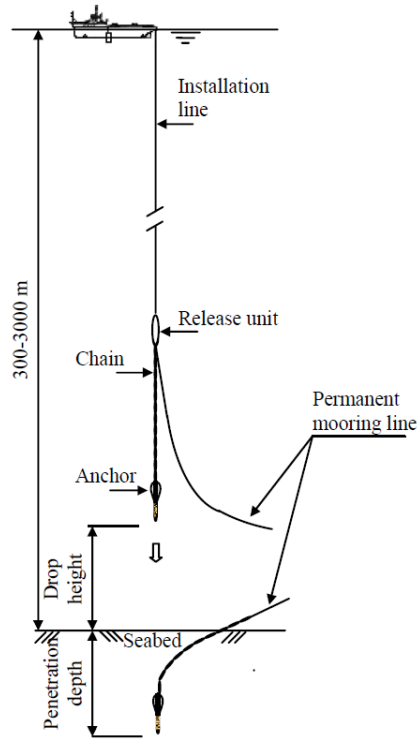


Figure 5. Deep penetrating anchor installation procedure (after Lieng, et al. 1999).

Lieng et al., (2000) numerically analyzed the anchor holding capacity using the finite element method (FEM). They considered three different soil models: total stress, critical state soil mechanics, and mobilized friction model. They found that in the undrained rapid loading condition, the holding capacity is not only influenced by the loading direction, but also the skin friction coefficient $\alpha = \tau_{max}/s_u$ selected in the simulation. Holding capacities will first increase and then decrease when loading angle with vertical direction is increasing from 0° (vertical) to 90° (horizontal). However, they found that, in the drained condition, the holding capacity is smaller when the anchor is inclined to the vertical direction. Additionally, the excess pore water pressure is related to the soil displacement due to the anchor penetration. Consolidation and the loading rate slightly influence the holding capacity.

O'Loughlin et al. (2004) designed experiments to study the behavior of deep penetrating anchors. They performed a series of centrifuge model tests to evaluate different methods of predicting anchor performance. Centrifuge modelling can accurately simulate prototype body force and stress conditions in a reduced scale model. They reported that soil resistance and drag coefficients predicted by existing models agreed with the centrifuge data. The scaled model was a torpedo anchor. Peak holding capacity can be computed as:

$$F_v = W_s + F_f + F_b \quad (23)$$

where W_s the submerged weight of the anchor, F_f the frictional resistance along the anchor shank and fluke walls, and F_b is the bearing resistance at top and bottom of the anchor shank.

The impact velocity can be calculated using Equation 24, and can reach values of approximately 30 m/s:

$$v_i = \sqrt{\frac{2W_b}{C_d A_p \rho_w}} \quad (24)$$

where C_d is the drag coefficient, W_b is the buoyant weight of the anchor in water, A_p is the projected area of the anchor, and ρ_w is the density of water. According to Freeman and Burdett (1986), the drag coefficient lies between $C_d = 0.039 + 0.0109L/d$ and $C_d = 0.030 + 0.0085L/d$ where L is anchor length and d is anchor diameter. A comparison of the drop height between measured and theoretical velocity is shown in Figure 6. The predicted values of embedment are based on the method proposed by True (1976) which considers both fluid drag resistance and viscous enhanced shearing resistance.

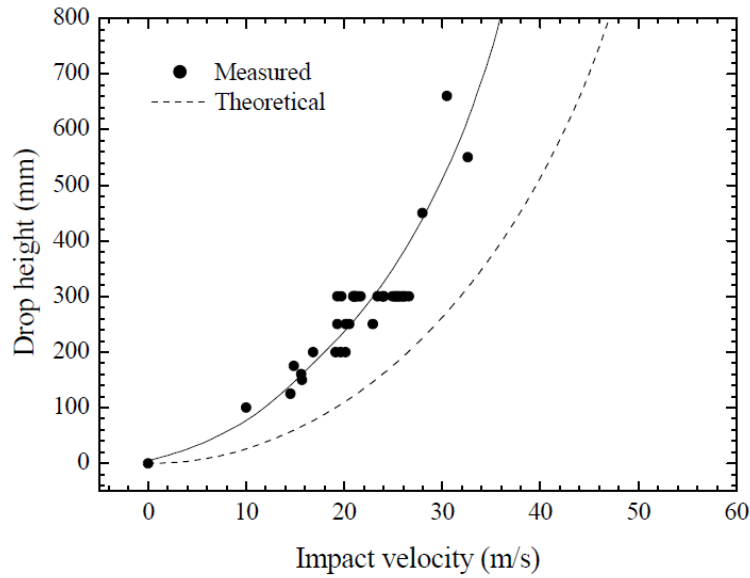


Figure 6. Drop height along with Impact velocity (after O’Loughlin et al. 2004)

DPA’s are not isolated entities in a MHK energy system. Their release will be influenced by the anchor line chain as well. Lieng et al. (2000) did a scaled (1:25) model test of the drop in the laboratory to determine the behavior of anchor lines and their influences on the anchor release. They found that the chain does not alter the anchor behavior during release due to the hydrodynamic drag on it. The anchor length influences the anchor behavior as it suspends the anchor.

3. DEM MODEL OF INTERFACE SHEAR

3.1. Model Overview

The geometry of the DEM model of the interface shear test is shown in Figure 7. The central region of the shaft passing through the cylindrical particulate assembly generates frictional resistance at two spatial scales. At the smaller of the two scales, there is sliding resistance due to Coulombic friction between a particle and the continuum counterface. At the larger scale, the shaft has a “zig-zag” texture that is approximately on the same scale as the particle size. We will refer to the smaller-scale effect as *friction* and the larger-scale effect as *roughness*; clearly, both contribute to ultimate shear resistance (commonly termed the *interface friction angle*). The rough shaft section is modeled as alternating conical frusta with user-defined geometry (Figure 8). The asperity angle (θ), tip-tip distance (h) and asperity peak (R) are all

defined as functions of median particle size d_{50} . The portion of the shaft outside of the rough central region has neither roughness nor friction and, thus does not contribute to the shear resistance of the shaft.

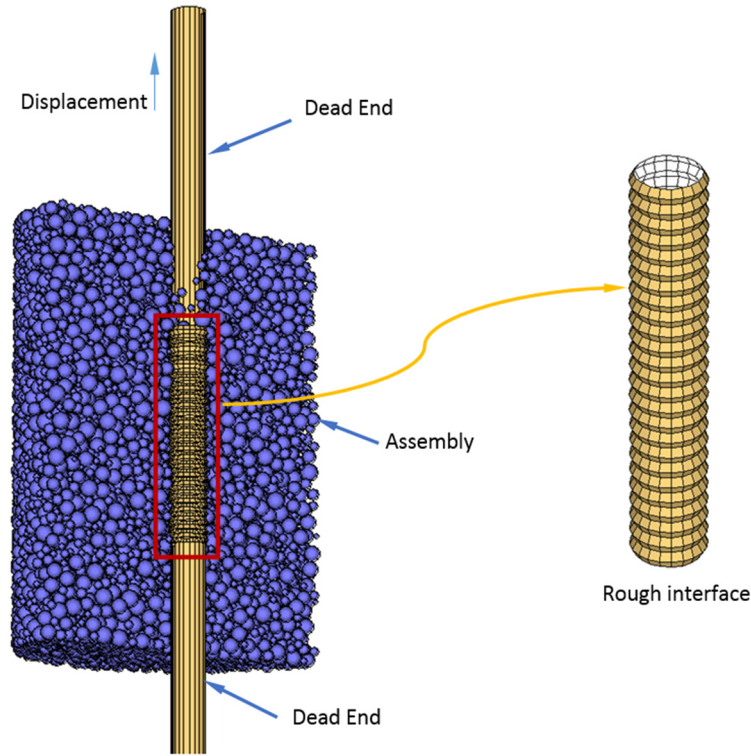


Figure 7. Geometry of the DEM model (particle assembly shown in section with half of particles removed to reveal continuum counterface). Note that the “dead ends” are frictionless and do not contribute to interface shearing resistance.

An assembly of polydisperse spherical particles is generated to fill the model volume between the shaft and the outer wall at a user-defined porosity. Mass scaling (e.g., Belheine et al. 2009; Evans and Valdes 2011) was employed to decrease simulation time; as such, the mean model particle diameter is $d_{50} = 0.5 \text{ m}$ and other model dimensions are scaled accordingly. Specifically, model height (H), model diameter (D), and shaft diameter (D_s) may be expressed in terms of d_{50} as $H/d_{50} = 24$, $D/d_{50} = 36$, and $D_s/d_{50} = 7.2$, respectively.

Previous research (Uesugi and Kishida 1988; Frost et al. 2004; Wang et al. 2007b), has found that shear band thickness in interface shear tests is approximately 8-10 median particle diameters. Thus, the radial distance between the shaft and the assembly boundary for the simulations in this study was set as $(D - D_s)/2d_{50} = 14.4$. In addition to the annular distance between the shaft and the assembly outer cylinder, Wang et al. (2007b) found that the friction between the particles and the walls is also significantly important. In this study, the friction between the particles and the shaft is treated as a user-defined variable and the outer wall friction is set to zero.

A numerical servo-control mechanism is used to isotropically consolidate the specimen such that it is in numerical equilibrium at a specified isotropic stress state ($\pm 0.5\%$) by adjusting the radius of the outer cylinder and the positions of the platens. The as-consolidated void ratio can be adjusted by varying the particles' and walls' friction coefficients during consolidation, with a higher friction value resulting in a

looser specimen. After consolidation, particle friction can be adjusted to assess the effects of particle friction on pullout resistance. Once the specimen is consolidated and equilibrated, the shaft is translated axially at a constant velocity. Two sets of boundary conditions are possible: (1) constant specimen volume (i.e., undrained shear); and (2) constant boundary tractions (i.e., drained shear). To monitor system response during shearing, the particle assembly is divided into four subzones, as shown in Figure 9. System behavior and state (e.g., coordination number, porosity, sliding friction and stress) in each subzone are monitored for further analysis. Normal and tangential forces are generated at contact points using a linear contact model. In the tangential direction, particle contacts are linear elastic-perfectly plastic and the failure force, T_f , is given as $T_f = \mu N$ where μ is the particle friction coefficient and N is the normal contact force. The interface shearing force is obtained by measuring the out-of-balance normal and shear forces opposite to the direction of shaft motion on all of the shaft walls and summing them.

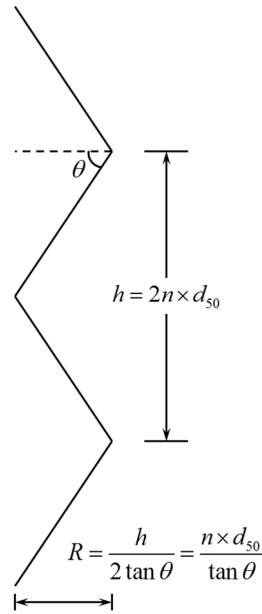


Figure 8. Shaft surface geometry. The tip-tip sawtooth length, h , is defined by a scale factor, n , the mean particle diameter, d_{50} , and an asperity angle, θ . The tip-trough relief (amplitude), R , is calculated from user defined variables.

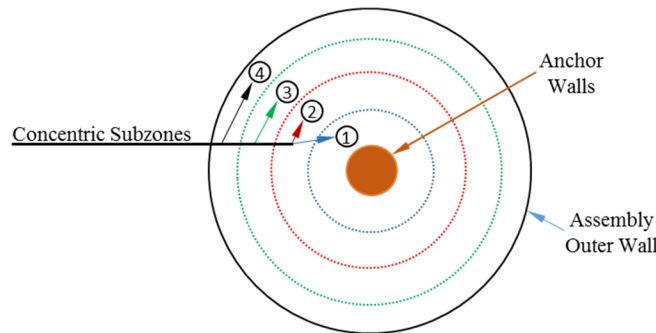


Figure 9. Subzones of zone between shaft and cylinder wall

3.2. Baseline System, Material, and Model Variables

The DEM model consists of particles and the model and shaft walls. A set of physically-admissible baseline material and model properties (Table 1) was selected to serve as a starting point for the simulations. Because the model does not purport to simulate system response on a particle-for-particle basis, it is typically necessary to slightly adjust these input parameters to more closely mimic observed physical behaviors. As a first step in determining appropriate – yet still physically admissible – model and material properties, the parameter space is mapped (see subsequent discussion) through a series of simulations, all of which are referenced back to the baseline parameter set. The properties presented in Table 1 below are consistent with silica sands in contact with rough steel or concrete interfaces.

Table 1. Material and model properties.

	Parameter	Value
Particles	Particle diameter ratio ⁽¹⁾ , d_{max}/d_{min} []	3
	Normal stiffness, k_n [N/m]	1×10^8
	Shear stiffness, k_s [N/m]	8×10^7
	Friction coefficient, μ []	0.31
	Density, ρ_s [kg/m ³]	2650
Model	Height, H [d_{50}]	24
	Diameter, D [d_{50}]	36
	Wall stiffness, k_w [N/m]	2×10^8
	Initial porosity []	0.40
Shaft Walls	Normal stiffness, k_{sn} [N/m]	2×10^8
	Shear stiffness, k_{ss} [N/m]	2×10^8
	Tip-tip distance, h [d_{50}]	0.2
	Asperity angle, θ [°]	45

⁽¹⁾Particle diameters are uniformly distributed between d_{min} and d_{max} .

3.3. Model Boundaries: Shear Zone Isolation

In an interface shear test, the region of the granular material immediately adjacent to the continuum counterface should undergo extensive failure while regions further from the counterface should remain relatively stable. Thus, one measure of the validity of the model geometry and shearing logic is the distribution of failure within the far field granular assembly (e.g., if the entire assembly enters into failure, the model would be considered to be too small). In a granular assembly, failure is the loss of particle-particle contacts, which manifests at the design scale as an assembly's inability to continue to carry load.

For the baseline simulation case, the fraction of sliding contacts (i.e., the fraction of particle-particle contacts that are in shear failure) in the four concentric subzones (Figure 9) was monitored. These results are presented in Figure 10, which shows that a higher percentage of contacts are in shear failure for the subzones closer to the shaft. This indicates a cascading failure beginning at the shaft and dissipating with

distance away from the continuum counterface, consistent with what has been observed in physical experiments.

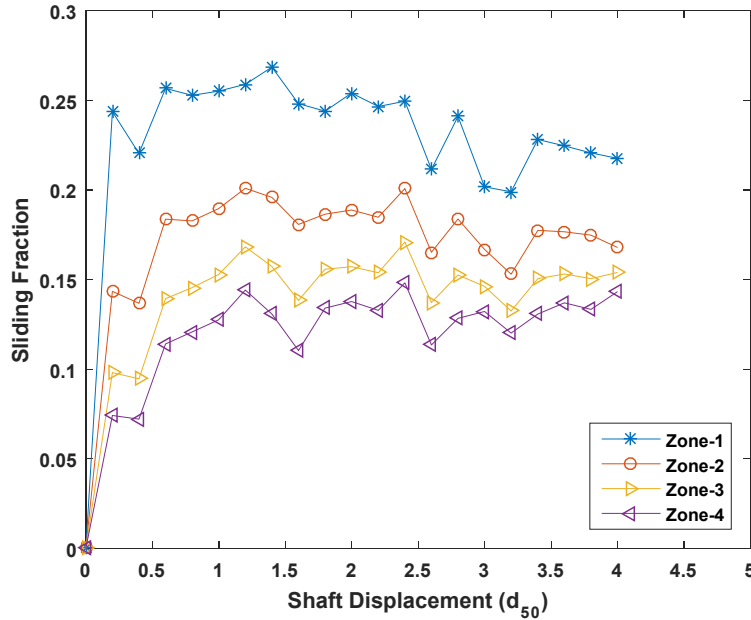


Figure 10. Sliding Fraction of different zones along with shaft displacement

4. RESULTS FROM PRELIMINARY PARAMETRIC STUDIES

4.1. Overview

A series of parametric simulations has been performed to assess the effects of varying X, Y, and Z on system response. In each case, a single model parameter is being isolated and varied across some range of physically appropriate values. These simulations serve two main purposes: (1) to elucidate problem physics by showing nontrivial variations in emergent response due to changes in physical inputs; and (2) to provide an intuitive check of overall model response – e.g., does interface friction angle increase with increasing counterface roughness? – based on a high-level understanding of the physical system.

4.2. Counterface Roughness

The first set of parametric simulations assesses the effects of a varying normalized roughness of the continuum counterface. Results from physical interface shear tests have previously been reported in the literature (Uesugi and Kishida 1986, 1986b, Jewell and Wroth 1987, Yoshimi et al 1988, Paikowsky et al 1995 and Fioranvante et al. 1999). In each of these studies, the definition of normalized roughness presented in Equation 2 was adopted. This is the definition that will be used hereinafter.

Referring to the experimental design of Uesugi and Kishida (1986b), the ratio (R/d_{50}) between the roughness R and median particle diameter d_{50} was set to approximately 0.02. Several values of surface roughness normalized by median particle diameter d_{50} will be presented in the report. The values of normalized roughness of the counterface that were considered are 0, 0.016, 0.02, 0.04, 0.1, 0.2, 0.4 and 1.0. Shear stress versus shaft displacement for the different surface roughness are shown in Figure 11.

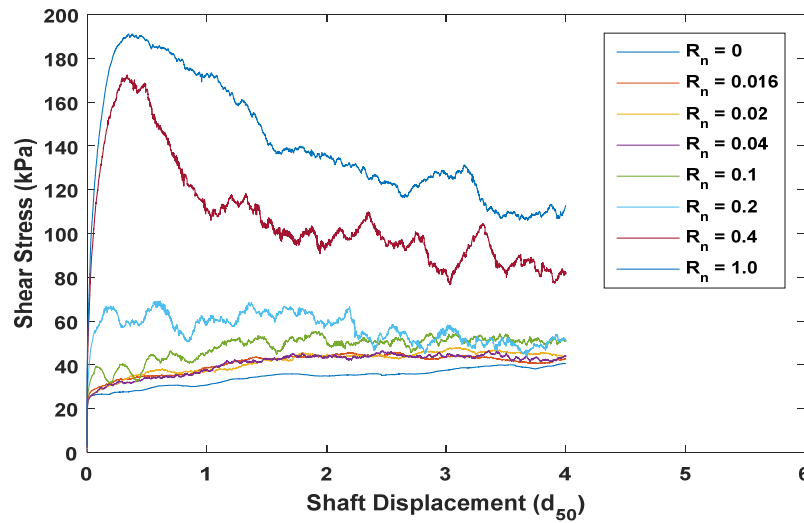


Figure 11. Shear stress along with shaft displacement with different surface roughness

Comparing system response for a range of counterface surface roughnesses, the higher the surface roughness, the larger the shear strength. There is significant softening behavior during pullout at higher surface roughness ($R_n = 0.4$ and $R_n = 1.0$). The occurrence of a well-defined peak strength (and the subsequent softening) is due to assembly redistribution, i.e., dilation. Specifically, the marked relief of the shaft ridges requires that there be significant rearrangement of particles within the shear zone, which serves to increase strength. Subsequent assembly redistribution leads to continuous softening as the system approaches steady state deformation. At low values of counterface roughness, system response is largely insensitive to small changes in roughness. This implies that shear failure at the interface is due to sliding rather than significant particle rearrangement. Clearly, this variation in response has significant design implications.

4.3. Counterface Friction Coefficient

The simulations presented above isolate the effects of varying shaft roughness for a constant shaft friction coefficient equal to the baseline friction of 0.31. Four other friction coefficients, 0.45, 0.55, 0.65 and 0.75 have also been considered (in these simulations, normalized roughness is constant at $R_n = 0.1$). The effects of shaft friction coefficient on the stress-displacement response of the system are shown in Figure 12. It is clear that higher the friction coefficients result in higher shear stresses. However, the effects of changing wall friction are not nearly as marked as those of changing roughness. Furthermore, increasing friction also has rapidly decreasing marginal returns, as shown in Figure 13. This conclusion has important design ramifications.

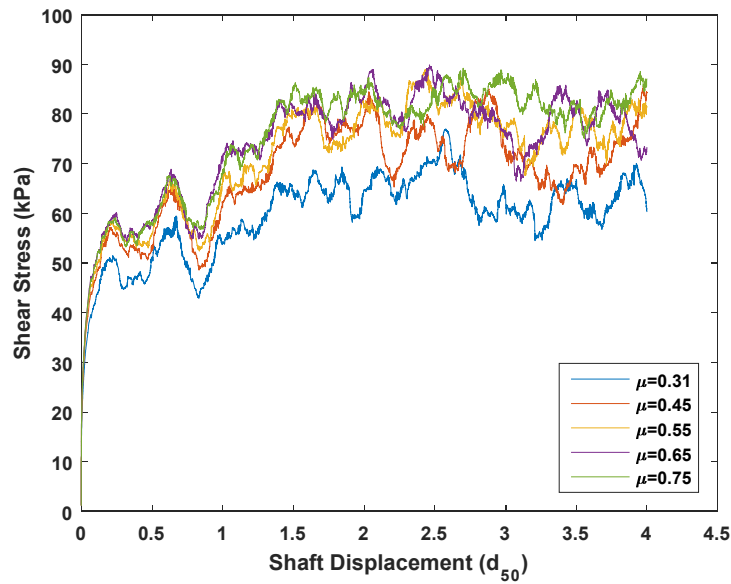


Figure 12. Shear stress along with shaft displacement with different shaft friction coefficients

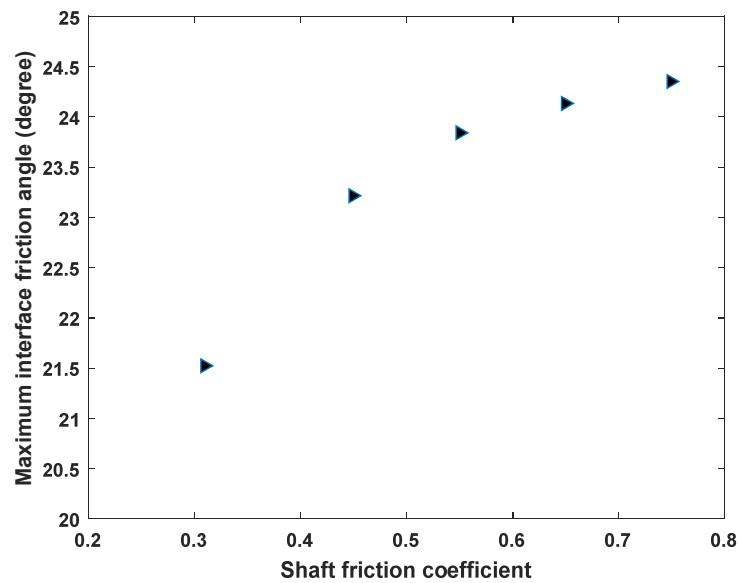


Figure 13. Maximum interface friction angle for shaft friction coefficients

4.4. Particle Stiffness

We have also performed preliminary simulations to assess the effects of particle stiffness on system response. Changing model particle stiffness would be a reflection of, e.g., changing particle mineralogy in the field. Appropriate values for particle stiffness are reasonably well defined for quartzitic sands. We are attempting to investigate the relationship between model input stiffness values and particle mineralogy.

The current set of three simulations all have ratios of particle normal to shear stiffness of approximately 1.2, consistent with classic Hertz-Mindlin theory for quartz spheres in contact at small deformation. Results are presented in Figures 14 and 15.

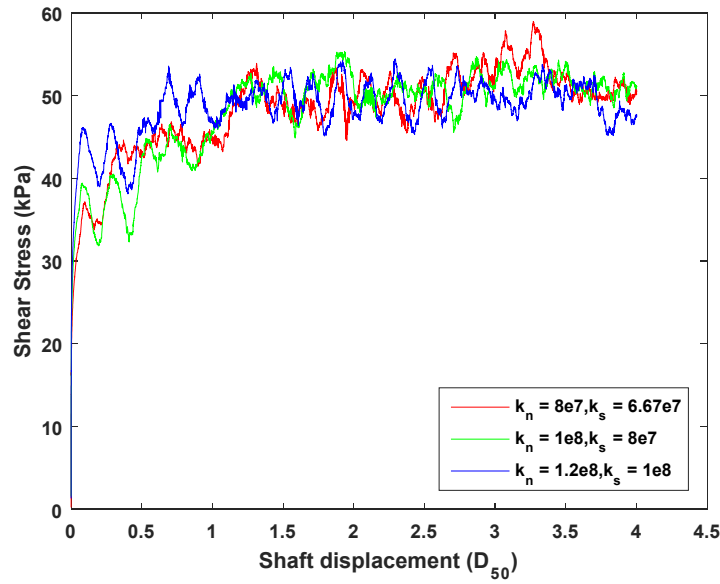


Figure 14. Shear stress along with anchor shaft displacement under different particle stiffness

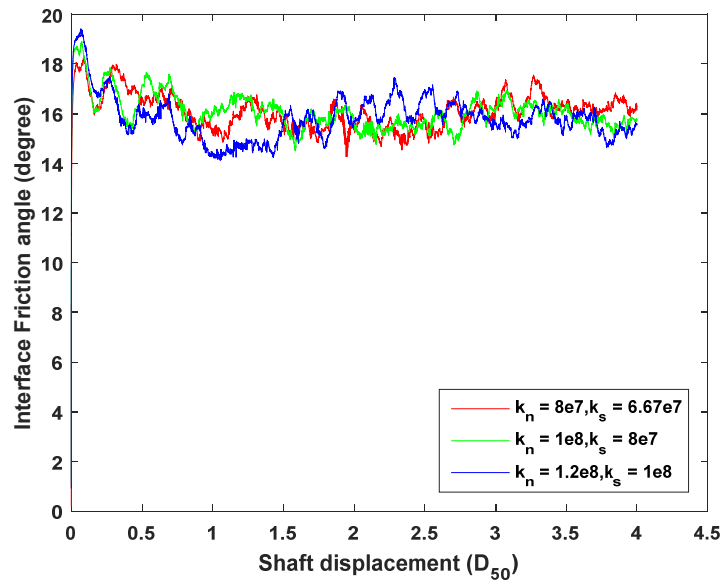


Figure 15. Interface friction angle along with shaft displacement under different particle stiffness

The results presented in Figures 14 and 15 are preliminary in that an appropriate range of stiffness values is still being defined. Stress-displacement results (Figure 14) do not indicate a significant difference across the range of stiffnesses considered. However, when volume change is considered (Figure 15), there is a clear empirical preference for higher peak friction angle with increasing particle stiffness. We anticipate that this is due to greater dilation in stiffer systems, but this has yet to be confirmed with micromechanical analyses. This work is ongoing.

5. SUMMARY AND PRELIMINARY CONCLUSIONS

A thorough review of existing literature on both numerical and physical characterization of granular-continuum interface behavior has been performed. A review of the literature on offshore foundations and

anchors is ongoing and was briefly summarized. Several aspects were found to influence the granular-continuum interface behavior, including counterface roughness and topography and granular material size, shape, and mineralogy.

With the help of the previous work related to interface shearing, a DEM model has been developed to simulate interface shearing behavior. We have presented the results of a series of simulations of varying counterface roughness, counterface friction coefficient, and particle stiffness. The DEM model produced similar trends as in the physical experiments: counterface roughness was found to have significant influence on the shear stress at yield, counterface coefficient of friction was found to have less significance on the interface shear stress. Because, conceptually speaking, friction is the shear resistance that occurs at a spatial scale much smaller than the median particle diameter and roughness is the shear resistance that manifests at the scale of the median particle diameter. Specific comparisons between DEM simulations and physical experiments are discussed in the Checkpoint 4.1.2 report.

Counterface topography, particle stiffness effects, and particle shape effects will be further explored moving forward. In addition, we will begin to perform and calibrate simulations of anchor pullout in free-surface granular assemblies, similar to those present at the seafloor.

6. REFERENCES

- Acar, Y. B., Durgunoglu, H. T., and Tumay, M. T. (1982). Interface properties of sand. *Journal of Geotechnical and Geoenvironmental Engineering*, 108(GT4).
- Bathurst, R. J., and Rothenburg, L. (1990). Observations on stress-force-fabric relationships in idealized granular materials. *Mechanics of Materials*, 9, 65–80.
- Belheine N., Plassiard J. P., Donze F. V., Darve F. and Seridi A. (2009). “Numerical simulation of drained triaxial test using 3D discrete element modeling.” *Computers and Geotechnics*, 36(1-2), 320-331.
- Clough, G. W., and Duncan, J. M. (1969). Finite Element Analyses of Port Allen and Old River Locks (No. TE-69-3). California Univ Berkeley Inst of Transportation and Traffic Engineering.
- Dove, J., Bents, D., Wang, J., and Gao, B. (2006). Particle-scale surface interactions of non-dilative interface systems. *Geotextiles and Geomembranes*, 24(3), 156–168.
- Dove, J. E., and Frost, J. D. (1999). Peak friction behavior of smooth geomembrane-particle interfaces. *Journal of Geotechnical and Geoenvironmental Engineering*, 125(7), 544-555.
- Dove, J. E., and Jarrett, J. B. (2002). Behavior of dilative sand interfaces in a geotribology framework. *Journal of Geotechnical and Geoenvironmental Engineering*, 128(1), 25–37.
- Drew, B., Plummer, A. R., and Sahinkaya, M. N. (2009). A review of wave energy converter technology. *Proceedings of the Institution of Mechanical Engineers, Part A: Journal of Power and Energy*, 223(8), 887-902.
- Evans, T.M. and Valdes J.R. (2011). “The microstructure of particulate mixtures in one -dimensional compression: numerical studies.” *Granular Matter*, 13, 657-669.
- Evgin, E., and Fakharian, K. (1996). Effect of stress paths on the behavior of sand- steel path. *Canadian Geotechnical Journal*, 33(6), 853–865.
- Frost, J. D., DeJong, J. T., & Recalde, M. (2002). Shear failure behavior of granular–continuum interfaces. *Engineering Fracture Mechanics*, 69(17), 2029-2048.

- Frost, J.D., G.L. Hebel, T.M. Evans, and J.T. DeJong. (2004). "Interface Behavior of Granular Soils," *Proceedings of the 9th ASCE Aerospace Division International Conference on Engineering, Construction, and Operations in Challenging Environments*, Houston, TX, USA, pp. 65-72.
- Hu, L., and Pu, J. (2004). Testing and Modeling of Soil-Structure Interface. *Journal of Geotechnical and Geoenvironmental Engineering*, 130(8), 981–960.
- Itasca Consulting Group. (2008). "PFC^{3D}: Particle flow code in three dimensions v4.0," Minneapolis, MN.
- Jensen, R. P., Bosscher, P. J., Plesha, M. E., and Edil, T. B. (1999). DEM simulation of granular media—structure interface: effects of surface roughness and particle shape. *International Journal for Numerical and Analytical Methods in Geomechanics*, 23(6), 531-547.
- Jensen, R. P., Edil, T. B., Bosscher, P. J., Plesha, M. E., and Kahla, N. B. (2001a). Effect of Particle Shape on Interface Behavior of DEM-Simulated Granular Materials. *International Journal of Geomechanics*, 1(1), 1–19.
- Jensen, R. P., Plesha, M. E., Edil, T. B., Bosscher, P. J., and Kahla, N. B. (2001b). DEM Simulation of Particle Damage in Granular Media — Structure Interfaces. *International Journal of Geomechanics*, 1(1), 21–39.
- Kulhawy, F. H., and Peterson, M. S. (1979). Behavior of sand-concrete interfaces. In *Proceedings of the 6th Panamerican Conference on Soil Mechanics and Geotechnical Engineering*, pp. 225-236.
- Lieng, J. T., Hove, F., and Tjelta, T. I. (1999). Deep Penetrating Anchor: Subseabed deepwater anchor concept for floaters and other installations. In *proceedings of the Ninth International Offshore and Polar Engineering Conference*. International Society of Offshore and Polar Engineers.
- Lieng, J. T., Kavli, A., Hove, F., and Tjelta, T. I. (2000). Deep penetrating anchor: further development, optimization and capacity verification. In *proceedings of the Tenth International Offshore and Polar Engineering Conference*. International Society of Offshore and Polar Engineers.
- Medeiros Jr, C. J. (2002). Low cost anchor system for flexible risers in deep waters. In *proceedings of Offshore Technology Conference*, Houston, Paper OTC 14151.
- O'Loughlin, C. D., Randolph, M. F., & Richardson, M. (2004). Experimental and theoretical studies of deep penetrating anchors. In *proceedings of Offshore Technology Conference*, Houston. Paper 16841.
- Potyondy, J. G. (1961). Skin friction between various soils and construction materials. *Géotechnique*, 11(4), 339-353.
- Randolph, M. F., and Gourvenec, S. (2011). *Offshore Geotechnical Engineering*. CRC Press, New York, NY.
- Rothenburg L. (1980). Micromechanics of idealized granular systems. Ph.D. thesis, Carleton University, Ottawa, Ontario, Canada.
- Uesugi, M., and Kishida, H. (1986a). Frictional Resistance at Yield between Dry Sand and Mild. *Soils and Foundations*, 26(4), 139–149.
- Uesugi, M., and Kishida, H. (1986b). Influential factors of friction between steel and dry sands. *Soils and Foundations*, 26(2), 33–46.
- Uesugi, M., and Kishida, H. (1988). Behavior of sand particles in sand-steel friction. *Soils and Foundations*, 28(1), 107–118.
- Wang, J., Dove, J. E., and Gutierrez, M. S. (2007a). Anisotropy-based failure criterion for interphase systems. *Journal of Geotechnical and Geoenvironmental Engineering*, 133(5), 599–608.

- Wang, J., Dove, J. E., and Gutierrez, M. S. (2007b). Discrete-continuum analysis of shear banding in the direct shear test. *Géotechnique*, 57(6), 513–526.
- Wang, J., Dove, J. E., and Gutierrez, M. S. (2007c). Determining particulate–solid interphase strength using shear-induced anisotropy. *Granular Matter*, 9(3-4), 231–240.
- Wang, J., Gutierrez, M. S., and Dove, J. E. (2007d). Numerical studies of shear banding in interface shear tests using a new strain calculation method. *International Journal for Numerical and Analytical Methods in Geomechanics*, 31(12), 1349–1366.
- Yoshimi, Y., and Kishida, T. (1981). A Ring Torsion Apparatus for Evaluating Friction between Soil and Metal Surfaces. *Geotechnical Testing Journal*, 4(4), 145–152.

APPENDIX A
SAMPLE INPUT SCRIPT

Generate Assembly

```

new
set random 112706
set log off
set max_ball 50000 ; modify to be close to expect number of particles
set gravity 0.0 0.0 0.0
set safety_fac = 0.1
set echo on
;
;-----
; Function to define test parameters and constants
;-----
;
def def_const
; -----
; wall constants
; -----
extend = 0.1
w_stiff = 2e8
ws_stiff = 0.0
wfric = 0.0
stiff_mul = 0.1
; -----
; Anchor constants
; -----
an_nstiff = 2e8
an_sstiff = 1e8
an_fric = 0.155
; -----
; particle type s constants
; -----
s_rho = 2650.0
s_fric = 0.31 ; actual particle friction
si_fric = 0.0 ; friction used at assembly to control porosity
sn_stiff = 1e8
ss_stiff = 8e7
dlos = 0.25
dhis = 0.75
s_color = 1
s_type = 1
; -----
; model constants
; -----
height = 12.0 ; along z axis
width = 18.0 ; diameter of cylindrical model space
poros = 0.40 ; porosity at assembly
; -----
; anchor/movement constants ; NOTE: User must confirm even integer number of walls.
; -----
a_size_ratio = 0.2 ; ratio of inner anchor diameter to model diameter
theta = 45.0 ; asperity angle, in degrees
_h = 0.05 ; the tip-to-trough tooth length, in model dimensions
a_top = 0.80 ; height of top of anchor teeth
a_bot = 0.20 ; height of bottom of anchor teeth
an_dis = 10.0 ; anchor displacement, in units of "teeth"
v_anchor = 0.1
file_inc = 1.0 ; frequency of save files, "teeth"
; -----
; consolidation constants
; -----
sig_tol = 0.005
conso_cycle_num = 0
srrreq = -100.0e3
szzreq = -100.0e3
; -----
; miscellaneous
; -----
wezz = 0
wezz_0 = 0
_bid0 = 0

```



```

n_spheres      = 250
n_zones        = 4
tot_spheres    = n_zones*n_spheres
fnum           = 0
end
;
;-----
; Generate walls and anchor
;-----
;
def make_walls
; Anchors
x_0 = 0.0
y_0 = 0.0

rad1 = a_size_ratio * width/2.0
rad2 = rad1 + _h/tan(theta*pi/180.0)

nw = round(height*(a_top - a_bot)/_h) ; NOTE: User must confirm that nw is an even integer.

deadend_top      = nw + 1
deadend_bottom   = nw + 2
cylinder_wall    = nw + 3
cylinder_top     = nw + 4
cylinder_bottom  = nw + 5

zz0 = a_bot*height;

loop j(1,nw/2)
  idn = 2*j - 1
  zz1 = zz0 + _h
  command
    wall type cylinder id=idn kn=an_nstiff ks=an_sstiff fr= an_fric &
    end1 (x_0,y_0,zz0) end2 (x_0,y_0,zz1) rad (rad1,rad2)
  end_command
  idn = idn + 1
  zz0 = zz1
  zz1 = zz1 + _h
  command
    wall type cylinder id=idn kn=an_nstiff ks=an_sstiff fr=an_fric &
    end1 (x_0,y_0,zz0) end2 (x_0,y_0,zz1) rad (rad2,rad1)
  end_command
  zz0 = zz1
end_loop

; a cylinder
rad_cy = 0.5 * width
z_0 = -height*extend
z_1 = height*(1.0+extend)
command
  wall type cylinder id=cylinder_wall kn=w_stiff ks=0.0 fr=0.0 &
  end1 (x_0,y_0,z_0) end2 (x_0,y_0,z_1) rad (rad_cy,rad_cy)
end_command

; deadend top cylinder
z_0 = a_top*height
z_1 = 1.5*height
command
  wall type cylinder id=deadend_top kn=w_stiff ks=0.0 fr=0.0 &
  end1 (x_0,y_0,z_0) end2 (x_0,y_0,z_1) rad (rad1,rad1)
end_command

; deadend bottom cylinder
z_0 = a_bot*height
z_1 = -0.5*height
command
  wall type cylinder id=deadend_bottom kn=w_stiff ks=0.0 fr=0.0 &
  end1 (x_0,y_0,z_0) end2 (x_0,y_0,z_1) rad (rad1,rad1)
end_command

; top plate

```

```

_x0 = -rad_cy*(1.0+2.0*extend)
_y0 = -rad_cy*(1.0+2.0*extend)
_z0 = height
_x1 = -rad_cy*(1.0+2.0*extend)
_y1 = rad_cy*(1.0+2.0*extend)
_z1 = height
_x2= rad_cy*(1.0+2.0*extend)
_y2 = rad_cy*(1.0+2.0*extend)
_z2 = height
_x3= rad_cy*(1.0+2.0*extend)
_y3 = -rad_cy*(1.0+2.0*extend)
_z3 = height
command
    wall id=cylinder_top kn=w_stiff ks=0.0 fr=0.0 face &
        (_x0,_y0,_z0) (_x1,_y1,_z1) (_x2,_y2,_z2) (_x3,_y3,_z3)
end_command

; bottom plate
_x0 = -rad_cy*(1.0+2.0*extend)
_y0 = -rad_cy*(1.0+2.0*extend)
_z0 = 0.0
_x1 = rad_cy*(1.0+2.0*extend)
_y1 = -rad_cy*(1.0+2.0*extend)
_z1 = 0.0
_x2= rad_cy*(1.0+2.0*extend)
_y2 = rad_cy*(1.0+2.0*extend)
_z2 = 0.0
_x3= -rad_cy*(1.0+2.0*extend)
_y3 = rad_cy*(1.0+2.0*extend)
_z3 = 0.0
command
    wall id=cylinder_bottom kn=w_stiff ks=0.0 fr=0.0 face &
        (_x0,_y0,_z0) (_x1,_y1,_z1) (_x2,_y2,_z2) (_x3,_y3,_z3)
end_command

end
;
;-----
;      Function to assemble the model
;-----
;
def assemble
    make_walls
    wall_addr
    wall_positions

    av1 = pi*height*rad1^2.0
    av2 = nw*pi*_h*(rad2-rad1)*(2.0*rad1+rad2)/3.0
    anchor_vol = av1 + av2
    tot_vol = height*pi*(rad_cy^2.0) - anchor_vol
    V_solid = tot_vol * (1.0 - poros)

    make_grains_1

    command
        set echo on
        prop kn=sn_stiff ks=ss_stiff fric=si_fric
        prop color=s_color
    end_command
end
;
;-----
;      Function to generate spheres
;-----
;
def make_grains_1
    vol = 0.0
    loop while vol < V_solid
        r_ball = 0.5*(dlos + urand*(dhis - dlos))
        grain_vol = (4.0/3.0)*(pi*r_ball^3.0)
        vol = vol + grain_vol
        r_in = rad2 + r_ball
    end
end

```

```

        r_out = rad_cy - r_ball
        _theta = 2.0*pi*urand
        _r = r_in + urand*(r_out - r_in)
        _x = x_0 + _r*cos(_theta)
        _y = y_0 + _r*sin(_theta)
        _z = r_ball + urand*(height - 2.0*r_ball)
        _bid0 = _bid0 + 1
        command
            ball id=_bid0 x=_x y=_y z=_z rad=r_ball dens=s_rho
        end_command
    end_loop
    ii = pre_cycle
end
;
;-----
; define wall address
;-----
;
def wall_addr
    wadd1 = find_wall(cylinder_wall)
    wadd2 = find_wall(cylinder_top)
    wadd3 = find_wall(cylinder_bottom)
    wadd4 = find_wall(deadend_bottom)
    wadd5 = find_wall(deadend_top)
end
;
;-----
;
def wall_positions
    w2x = w_x(wadd2)
    w2y = w_y(wadd2)
    w2z = w_z(wadd2) + height
    w3x = w_x(wadd3)
    w3y = w_y(wadd3)
    w3z = w_z(wadd3)
    w4x = w_x(wadd4)
    w4y = w_y(wadd4)
    w4z = w_z(wadd4)
end
;
;-----
; Delete and balls that have escaped
;-----
;
def del_balls
    wall_positions
    bp = ball_head
    loop while bp # null
        del_flag = 0
        bnext = b_next(bp)
        radial_loc = sqrt(b_x(bp)^2 + b_y(bp)^2)
        bz = b_z(bp)
        if radial_loc > w_radendl(wadd1)
            del_flag = 1
        else
            if radial_loc < rad1
                del_flag = 1
            else
                if bz > w2z
                    del_flag = 1
                else
                    if bz < w3z
                        del_flag = 1
                    endif
                endif
            endif
        endif
        if del_flag > 0
            del_flag = 0
            ii = b_delete(bp)
            totdel = totdel + 1
        endif
    endloop
end

```

```

        endif
        bp = bnext
    end_loop
end
;
;-----
; Assemble the model, cycle to equilibrium, save the results
;-----
;
def_const
set echo off
assemble

set logfile iface_GSD.txt
set log on overwrite
print ball
set log off

cycle 20000 calm 5
solve
del_balls
call color_all_balls.dat
sav iface_assem.sav

call iface_consol.dat

```

Consolidate

```

new
restore iface_assem.sav
;
;-----
;
def consol_ss ; determine average stress and strain at walls
    new_rad1 = w_radend1(wadd1)
    rdif = new_rad1-rad_cy;
    zdif = w_z(wadd2)-w_z(wadd3)
    new_height = height+zdif
    wsrr = -w_radfob(wadd1) / (new_height * 2.0 * pi * new_rad1)
    wszz = 0.5*(w_zfob(wadd3) - w_zfob(wadd2)) / (pi * (new_rad1)^2.0)
    werr = 2.0 * rdif / (rad_cy + new_rad1)
    wezz = 2.0 * zdif / (height + new_height)
    wevol = wezz + 2.0 * werrf
end
;
;-----
;
def consol_gain ; determine servo gain parameters
    alpha = 0.5
    avg_stiff = 0
    cp = contact_head ; find avg. number of contacts on cylinder
    loop while cp # null
        if c_gobj2(cp) = wadd1
            avg_stiff = avg_stiff + c_kn(cp)
        end_if
        cp = c_next(cp)
    end_loop
    rg = alpha * new_height * pi * new_rad1 * 2.0 / (avg_stiff * tdel)
    avg_stiff = 0
    cp = contact_head ; find avg. number of contacts on top/bottom walls
    loop while cp # null
        if c_gobj2(cp) = wadd2
            avg_stiff = avg_stiff + c_kn(cp)
        end_if
        if c_gobj2(cp) = wadd3
            avg_stiff = avg_stiff + c_kn(cp)
        end_if
        cp = c_next(cp)
    end_loop
    gz = 2.0 * alpha * pi * new_rad1^2.0 / (avg_stiff * tdel)
end

```

```

;
;-----
;
def consol_servo
    while_stepping
        if consol_on = 0
            exit
        end_if
        consol_ss
        udr = rg * (wsrr - srrreq)
        w_radvel(wadd1) = -udr
        if z_servo = 1
            udz = gz * (wszz - szzreq)
            w_zvel(wadd2) = -udz
            w_zvel(wadd3) = udz
        end_if
    end
;
;-----
;
def consol_iterate
    loop while 1 # 0
        consol_gain
        if abs((wsrr - srrreq) / srrreq) < sig_tol then
            if abs((wszz - szzreq) / szzreq) < sig_tol then
                exit
            end_if
        end_if
        command
            cycle 100
            print wsrr, wszz, udz, udr
        end_command
    end_loop
end
;
;-----
;
def consolidate
    z_servo = 1
    consol_on = 1
    consol_ss
    loop while 1 # 0
        conso_cycle_num = conso_cycle_num + 1
        del_balls
        consol_iterate
        command
            solve
        end_command
        consol_ss
        if abs((wsrr - srrreq) / srrreq) < sig_tol then
            if abs((wszz - szzreq) / szzreq) < sig_tol then
                consol_on = 0
                del_balls
                exit
            end_if
        end_if
    end_loop
end
;
;-----
;change wall stiffness
;-----
;
def cws
    w_kn(wadd1) = stiff_mul*w_kn(wadd1)
    w_kn(wadd2) = stiff_mul*w_kn(wadd2)
    w_kn(wadd3) = stiff_mul*w_kn(wadd3)
end
;
;-----
;

```

```

cws
consolidate

save iface_consol.sav

call iface_shear.dat

```

Shear

```

new
restore iface_consol.sav

;-----
;Create measurement spheres
;-----
def make_spheres
    wall_positions
    r_ms = (w_radendl(waddl)-rad2)/(2.0*n_zones)
    loop nn (1,n_zones)
        _rr = rad2 + (2.0*nn-1.0)*r_ms
        msid0 = 1 + (nn - 1)*n_spheres
        msidl = msid0 + n_spheres - 1
        loop id_ms (msid0, msidl)
            _theta = 2.0*pi*urand
            xx = _rr * cos(_theta)
            yy = _rr * sin(_theta)
            zz = height*a_bot + w4z + r_ms + urand*(height*(a_top - a_bot) - 2.0*r_ms)
            command
                measure id id_ms x xx y yy z zz rad r_ms
            end_command
        end_loop
    end_loop
end

;-----
def ms_info
    array ms_para(tot_spheres,15)
    mp = circ_head
    loop msid (1,tot_spheres)
        oo = measure(mp,1)
        pp = measure(mp,2)
        ms_para(msid,1) = m_x(mp)
        ms_para(msid,2) = m_y(mp)
        ms_para(msid,3) = m_z(mp)
        ms_para(msid,4) = m_poros(mp)
        ms_para(msid,5) = m_coord(mp)
        ms_para(msid,6) = m_s11(mp)
        ms_para(msid,7) = m_s12(mp)
        ms_para(msid,8) = m_s13(mp)
        ms_para(msid,9) = m_s21(mp)
        ms_para(msid,10) = m_s22(mp)
        ms_para(msid,11) = m_s23(mp)
        ms_para(msid,12) = m_s31(mp)
        ms_para(msid,13) = m_s32(mp)
        ms_para(msid,14) = m_s33(mp)
        ms_para(msid,15) = m_sfrac(mp)
        mp = m_next(mp)
    end_loop
end

;
;-----
;
def ashow
    dum=out('MS output for '+string(tot_spheres)+' divided equally among '+string(n_zones)+'
    zones.')
    loop mm (1,tot_spheres)
        msg = ' '
        loop n (1,15)
            msg = msg + ' ' +string(ms_para(mm,n))
        end_loop
        dum = out(msg)
    end_loop
end

```

```

end
;
;-----
;
def get_ss
    new_rad1 = w_radend1(wadd1)
    rdif = new_rad1-rad_cy;
    zdif = w_z(wadd2)-w_z(wadd3)
    new_height = height+zdif
    wsrr = -w_radfob(wadd1) / (new_height * 2.0 * pi * new_rad1)
    wszz = 0.5*(w_zfob(wadd3) - w_zfob(wadd2)) / (pi * (new_rad1)^2.0)
    werr = 2.0 * rdif / (rad_cy + new_rad1)
    wezz = 2.0 * zdif / (height + new_height)
    wevol = wezz + 2.0 * werrf
end
;
;-----
;
def get_gain
    alpha = 0.5
    avg_stiff = 0
    cp = contact_head
    loop while cp # null
        if c_gobj2(cp) = wadd1
            avg_stiff = avg_stiff + c_kn(cp)
        end_if
        cp = c_next(cp)
    end_loop
    rg = alpha * new_height * pi * new_rad1 * 2.0 / (avg_stiff * tdel)
    avg_stiff = 0
    cp = contact_head
    loop while cp # null
        if c_gobj2(cp) = wadd2
            avg_stiff = avg_stiff + c_kn(cp)
        end_if
        if c_gobj2(cp) = wadd3
            avg_stiff = avg_stiff + c_kn(cp)
        end_if
        cp = c_next(cp)
    end_loop
    gz = 2.0 * alpha * pi * new_rad1^2.0/ (avg_stiff * tdel)
end
;
;-----
;
def servo
    while_stepping
        if consol_on = 0
            exit
        end_if
        udr = rg * (wsrr - srrreq)
        w_radvel(wadd1) = -udr
        if z_servo = 1
            udz = gz * (wszz - szzreq)
            w_zvel(wadd2) = -udz
            w_zvel(wadd3) = udz
        end_if
    end
;
;-----
;
def get_anchor_pointers
    array anchor_points(nw)
    nwp = 0
    wp = wall_head
    loop while wp # null
        if w_id(wp) <= nw
            nwp = nwp + 1
            anchor_points(nwp) = wp
        end_if
        wp = w_next(wp)
    end

```

```

        end_loop
end
;
;-----
;
def start_anchor
    w_zvel(wadd4) = v_anchor
    w_zvel(wadd5) = v_anchor
    loop n (1,nw)
        w_zvel(anchor_points(n)) = v_anchor
    end_loop
end
;
;-----
;
def iface_shear
    nt = 0.0
    ;z_flag = _h * file_inc
    command
        get_gain
        get_ss
        cyc 100
        print strr, strz, ster, stez, zdis, pof, rg, gz, udr, udz
        set hist_rep 100
    end_command
    loop while zdis < 2.0
        command
            get_gain
            get_ss
            cyc 100
            print strr, strz, ster, stez, zdis, pof, rg, gz, udr, udz
        end_command
        if zdis >= nt + 0.1;
            fnum = fnum + 1
            nt = nt + 0.1;
            z_flag = z_flag + _h * file_inc
            fname1 = 'iface_shear_'+string(fnum)+'.sav'
            fname2 = 'iface_shear_ms_'+string(fnum)+'.out'
            make_spheres
            ms_info
            command
                save fname1
                set logfile fname2
                set log on overwrite
                ashow
                set log off
            end_command
        end_if
    end_loop
end
;
;-----
;
def set_ini
    werr_0 = werr
    wezz_0 = wezz
end
;
;-----
;
def pof
    pullout_force = 0.0
    nn_force = 0.0
    ss_force = 0.0
    loop n (1,nw)
        pullout_force = pullout_force + w_zfob(anchor_points(n))
    end_loop
    cp = contact_head
    loop while cp # null
        pid = c_ball2(cp)
    end_loop
end

```



```

        if pointer_type(pid) = 101
            if w_id(pid) <= nw
                nn_force = nn_force + c_nforce(cp)
                ss_force = ss_force + c_zsforce(cp)
            end_if
        end_if
        cp = c_next(cp)
    end_loop
    strr = wsrr ; radial confining stress
    strz = wszz ; axial confining stress
    ster = werr - werr_0 ; radial strain
    stez = wezz - wezz_0 ; axial strain
    zdis = w_z(anchor_points(1)) ; anchor displacement
    pof = pullout_force ; anchor pull-out force
    nf = nn_force ; normal force of the anchor
    sf = ss_force + nn_force*cos(theta) ; shear force using contact forces
end
;
;-----
;
def quiet_wall ;set the velocity of walls to be zero after consolidation
    w_radvel(wadd1) = 0.0
    w_zvel(wadd2) = 0.0
    w_zvel(wadd3) = 0.0
end
;
;-----
;
; Set max friction as the interface friction coefficient
def set_max
    loop n (1,nw)
        command
            wall id n maxfric on
        end_command
    end_loop
end
;-----

prop fric=s_fric ; Assign actual particle friction before shear
set_max
get_anchor_pointers
quiet_wall
set_ini
set consol_on = 1
set hist_rep 1
his pof
his zdis
his nf
his sf
his strr
his strz
his ster
his stez
his diagnostic muf
his diagnostic mcf
make_spheres
ms_info
save iface_shear_0.sav
set logfile iface_shear_ms_0.out
set log on overwrite
ashow
set log off
start_anchor
iface_shear
hist write 1 2 3 4 5 6 7 8 file iface_shear.his
hist write 9 10 file iface_shear_unbal.his

```